Solution-Processable α,ω-Distyryl Oligothiophene Semiconductors with Enhanced Environmental Stability

Clayton E. Mauldin,[†] Kanan Puntambekar,[‡] Amanda R. Murphy,[†] Frank Liao,[‡] Vivek Subramanian,[‡] Jean M. J. Fréchet,*[,†] Dean M. DeLongchamp,[§] Daniel A. Fischer,[§] and Michael F Toney[⊥]

Department of Chemistry and Department of Electrical Engineering and Computer Sciences, University of California, Berkeley, California 94720-1460, Material Sciences Division, Lawrence Berkeley National Laboratory, Berkeley, California, Polymers Division, National Institute of Standards and Technology, Gaithersburg, Maryland 20899, and Stanford Synchrotron Radiation Laboratory, Menlo Park, California

Received January 28, 2009. Revised Manuscript Received March 4, 2009

We describe the rational design of oligothiophene semiconductors to facilitate solution-based fabrication of environmentally stable organic field-effect transistors (OFETs). Ultrathin films of α,ω-distyryl quaterthiophene (**DS4T**), pentathiophene (**DS5T**), and sexithiophene (**DS6T**) were prepared via solution processing to probe the effect of styryl end groups, oligomer length, and thin film structure on air stability. These films were prepared via solution deposition and thermal annealing of precursors featuring thermally labile ester solubilizing groups. A detailed study of the thin film structure was performed using atomic force microscopy (AFM), near-edge X-ray absorption fine structure (NEXAFS) spectroscopy, and grazing incidence X-ray diffraction (GIXD). Functional OFETs were obtained for **DS5T** and **DS6T** and have, respectively, hole mobilities of 0.051 and 0.043 $cm^2/(V\ s)$ and on/off ratios of 1×10^5 to 1×10^6, whereas **DS4T** OFETs failed to function because of poor film continuity. The effect of both short-term and long-term exposure to air is tracked in OFETs revealing remarkable stability for both **DS5T** and **DS6T**. This stability is attributed to the elimination of reactive sites in α,ω-distyryl oligothiophenes and suggests that careful choice of end-group structure can stabilize these molecules against oxidative degradation.

Introduction

Conjugated small molecules and polymers that show promise as organic semiconductors are typically limited by their sensitivity to ambient conditions. In particular, positive hole-transporting materials are believed to be susceptible to oxidation by molecular oxygen that decreases the charge mobility (μ) of the materials and degrades on/off ratios by increasing the off-currents in organic field-effect transistors (OFETs).[1−3] As a result, much work has focused on improving the stability of these materials, typically by increasing the oxidation potential of the molecules to preserve high on/off ratios.[4−6] Although this strategy has proven to be successful, theoretically it can adversely affect charge injection by pushing the HOMO energy of the molecules away from the Fermi level of commonly used gold electrodes.[6−8] Alternatively, the molecular structure of these conjugated materials can be rationally designed to minimize sensitivity to common degradation pathways under ambient conditions. However, further elucidation and validation of these degradation pathways is necessary for this method to be effective.

One such approach is suggested by the exceptional stability of α,ω-distyryl quarterthiophene (**DS4T**) to ambient conditions.[9] This material formed the active layer in OFETs that provided stable operation under ambient conditions for a period of 17 months, which greatly exceeds the stability of unfunctionalized oligothiophenes. The stabilizing effect of terminal styryl groups appears unrelated to the oxidation potential of the material because styryl end groups actually increase the HOMO level of the molecules relative to the parent oligothiophenes. Therefore, the origin of the stability of **DS4T** to ambient conditions and oxygen in particular is unclear. Specifically, the aforementioned results suggest that the styryl end groups may somehow have a stabilizing effect on the delocalized π-system so that the stability of **DS4T** is a unique property of that structure as a whole. Nevertheless,

* Corresponding author. E-mail: frechet@berkeley.edu.
[†] Department of Chemistry, University of California, Berkeley, and Lawrence Berkeley National Laboratory.
[‡] Department of Electrical Engineering and Computer Science, Univeristy of California, Berkeley.
[§] National Institute of Standards and Technology.
[⊥] Stanford Synchotron Radiation Laboratory.

(1) Meijer, E. J.; Detcheverry, C.; Baesjou, P. J.; van Veenendaal, E; de Leeuw, D. M.; Klapwijk, T. M. *J. Appl. Phys.* **2003**, *93*, 4831–4835.
(2) Pannemann, C.; Diekmann, T.; Hilleringmann, U. *J. Mater. Res.* **2008**, *19*, 1999–2002.
(3) Zhenan, B.; Ananth, D.; Andrew, J. L. *Appl. Phys. Lett.* **1996**, *69*, 4108–4110.
(4) Meng, H.; Bao, Z.; Lovinger, A. J.; Wang, B. C.; Mujsce, A. M. *J. Am. Chem. Soc.* **2001**, *123*, 9214–9215.
(5) Murphy, A. R.; Liu, J.; Luscombe, C.; Kavulak, D.; Fréchet, J. M. J.; Kline, R. J.; McGehee, M. D. *Chem. Mater.* **2005**, *17*, 4892–4899.
(6) Payne, M. M.; Parkin, S. R.; Anthony, J. E.; Kuo, C. C.; Jackson, T. N. *J. Am. Chem. Soc.* **2005**, *127*, 4986–4987.
(7) Abkowitz, M.; Facci, J. S.; Rehm, J. *J. Appl. Phys.* **1998**, *83*, 2670–2676.
(8) Shen, Y; Ahmad, R. H. *ChemPhysChem* **2004**, *5*, 16–25.
(9) Videlot-Ackermann, C.; Ackermann, J.; Brisset, H.; Kawamura, K.; Yoshimoto, N.; Raynal, P.; ElKassmi, A.; Fages, F. *J. Am. Chem. Soc.* **2005**, *127*, 16346–16347.

10.1021/cm900267v CCC: $40.75
Published on Web 04/08/2009

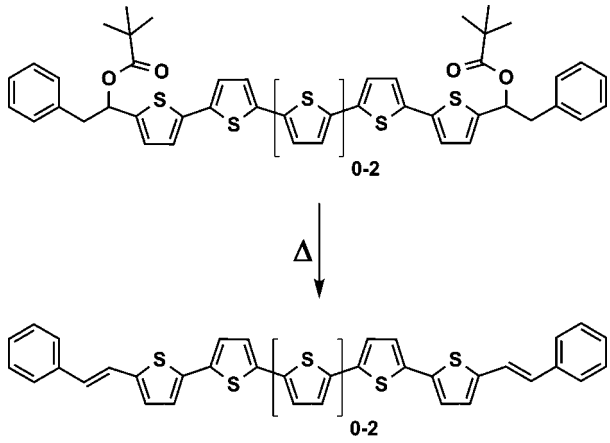

Figure 1. Thermolysis of ester solubilizing groups generates α,ω-distyryl oligothiophenes.

a better understanding of this stability is relevant for the structural design of oligothiophenes, which are synthetically versatile and therefore widely utilized organic semiconductors.[10−19]

To gain further insight into the stabilizing effect of styryl end groups on oligothiophenes, we prepared thermal precursors to α,ω-distyryl quarterthiophene (**DS4T**), pentathiophene (**DS5T**), and sexithiophene (**DS6T**). These thermal precursors feature bulky esters that inhibit crystallization of the oligomers and render them readily soluble. Upon thermal annealing, elimination of the esters initiates a reorganization of an initially amorphous film into a polycrystalline film[20,21] of α,ω-distyryl oligothiophenes. This structural transformation is shown in Figure 1.

We chose to prepare films of these α,ω-distyryl oligothiophenes through thermal removal of ester solubilizing groups as the high solubility of the precursor oligothiophenes allows facile material purification. Numerous strategies exist for solubilizing conjugated small molecules,[22,23] but importantly, this method allows simple deposition of ultrathin films via spin-coating and thermal annealing. As a result, the first few monolayers of conjugated oligomers responsible for charge transport in OFETs are directly exposed to ambient conditions with little of the self-encapsulation that could play a role in the stability of thicker films. Here we present the synthesis and thermal characterization of precursors to α,ω-distyryl oligothiophenes (**preDS4T**, **preDS5T**, and **preDS6T**). Analysis of thermally prepared **DS4T** by matrix-assisted laser desorption ionization -time-of-flight mass spectrometry (MALDI-TOF) reveals the clean thermal conversion of **preDS4T** to the desired styryl terminated product, which corresponds to a red-shift in the visible light absorption spectrum of the material. Structural and morphological characterization by atomic force microscopy (AFM), grazing incidence X-ray diffraction (GIXD), and near edge X-ray absorption fine structure (NEXAFS) spectroscopy of solution-processed films of the series of oligomers is presented. The materials are used as the active layer in field-effect transistor devices demonstrating the enhanced stability to ambient conditions attributable to the terminal styryl groups appended to the oligothiophene core.

Results

Synthesis. The symmetry of the target molecules allowed formation of each oligothiophene from a single coupling partner. Preparation of coupling partner **4** shown in Scheme 1 began with a Friedel−Crafts acylation of 2,2′-bithiophene with phenylacetyl chloride to yield ketone **1**. The ketone **1** is then converted to the corresponding alcohol **2** by reduction with lithium aluminum hydride. The alcohol **2** is then esterified to compound **3** using trimethylacetyl chloride with dimethylaminopyridine as the catalyst. The final step in the synthesis of the coupling partner is bromination with *N*-bromosuccinimide to generate **4**.

Each precursor oligomer was prepared by varying the linking strategy as shown in Scheme 1. Treatment of **4** with bis(pinacolato)diboron along with catalytic $Pd(PPh_3)_2Cl_2$ and excess potassium acetate led to formation of **preDS4T**. Treatment of **4** with 2,5-bis(trimethylstannyl)thiophene and catalytic $Pd(PPh_3)_2Cl_2$ provided a precursor oligomer to α,ω-distyryl pentathiophene (**preDS5T**), and an analogous cross-coupling utilizing 5,5′-bis(tributylstannyl)-[2,2′]bithiophene provided a precursor oligomer to α,ω-distyryl sexithiophene (**preDS6T**).

Thermogravimetric Analysis. For α,ω-distyryl oligothiophenes to be generated from the precursor oligomers, loss of the ester solubilizing groups (Figure 1) must occur during thermal annealing. Thermogravimetric analysis (TGA) shows the weight loss corresponding to cleavage of the solubilizing groups for the series of precursor oligomers (**preDS4T**, **preDS5T**, and **preDS6T**). The TGA data shown in Figure 2 for **preDS4T** and **preDS5T** demonstrates that thermal removal of the solubilizing groups is complete at 200 °C, whereas a higher temperature (225 °C) is required to effect removal of the ester solubilizing groups of **preDS6T**. Because the TGA data show a clear step pattern with a flat region from about 200−225 °C to 350−400 °C, thermal annealing of films within this temperature range results in

(10) Spada, G. P.; Lena, S.; Masiero, S.; Pieraccini, S.; Surin, M.; Samori, P. *Adv. Mater.* **2008**, *20*, 2433–2438.
(11) Wang, Z. S.; Koumura, N.; Cui, Y.; Takahashi, M.; Sekiguchi, H.; Mori, A.; Kubo, T.; Furube, A.; Hara, K. *Chem. Mater.* **2008**, *20*, 3993–4003.
(12) Zotti, G.; Vercelli, B.; Berlin, A. *Acc. Chem. Res.* **2008**, *41*, 1098–1109.
(13) Benincori, T.; Capaccio, M.; De Angelis, F.; Falciola, L.; Muccini, M.; Mussini, P.; Ponti, A.; Toffanin, S.; Traldi, P.; Sannicolo, F. *Chem.—Eur. J.* **2008**, *14*, 459–471.
(14) Henderson, J. C.; Kiya, Y.; Hutchison, G. R.; Abruna, H. D. *J. Phys. Chem. C* **2008**, *112*, 3989–3997.
(15) Ie, Y.; Umemoto, Y.; Okabe, M.; Kusunoki, T.; Nakayama, K.; Pu, Y. J.; Kido, J.; Tada, H.; Aso, Y. *Org. Lett.* **2008**, *10*, 833–836.
(16) Nakamura, T.; Araki, Y.; Ito, O.; Takimiya, K.; Otsubo, T. *J. Phys. Chem. A* **2008**, *112*, 1125–1132.
(17) You, C.-C.; Espindola, P.; Hippius, C.; Heinze, J.; Würthner, F. *Adv. Funct. Mater.* **2007**, *17*, 3764–3772.
(18) PonceOrtiz, R.; Casado, J.; Hernandez, V.; Navarette, J. T.; Viruela, P. M.; Orti, E.; Takimiya, K.; Otsubo, T. *Angew. Chem., Int. Ed.* **2007**, *46*, 9057–9061.
(19) Barbarella, G.; Melucci, M. *Adv. Mater.* **2005**, *17*, 1581–1593.
(20) Murphy, A. R.; Fréchet, J. M. J.; Chang, P.; Lee, J.; Subramanian, V. *J. Am. Chem. Soc.* **2004**, *126*, 1596–1597.
(21) Murphy, A. R.; Chang, P. C.; VanDyke, P.; Liu, J.; Fréchet, J. M. J.; Subramanian, V.; DeLongchamp, D. M.; Sambasivan, S.; Fischer, D. A.; Lin, E. K. *Chem. Mater.* **2005**, *17*, 6033–6041.
(22) Allard, S.; Forster, M.; Souharce, B.; Thiem, H.; Scherf, U. *Angew. Chem., Int. Ed.* **2008**, *47*, 4070–4098.
(23) Murphy, A. R.; Fréchet, J. M. J. *Chem. Rev.* **2007**, *107*, 1066–1096.

Scheme 1

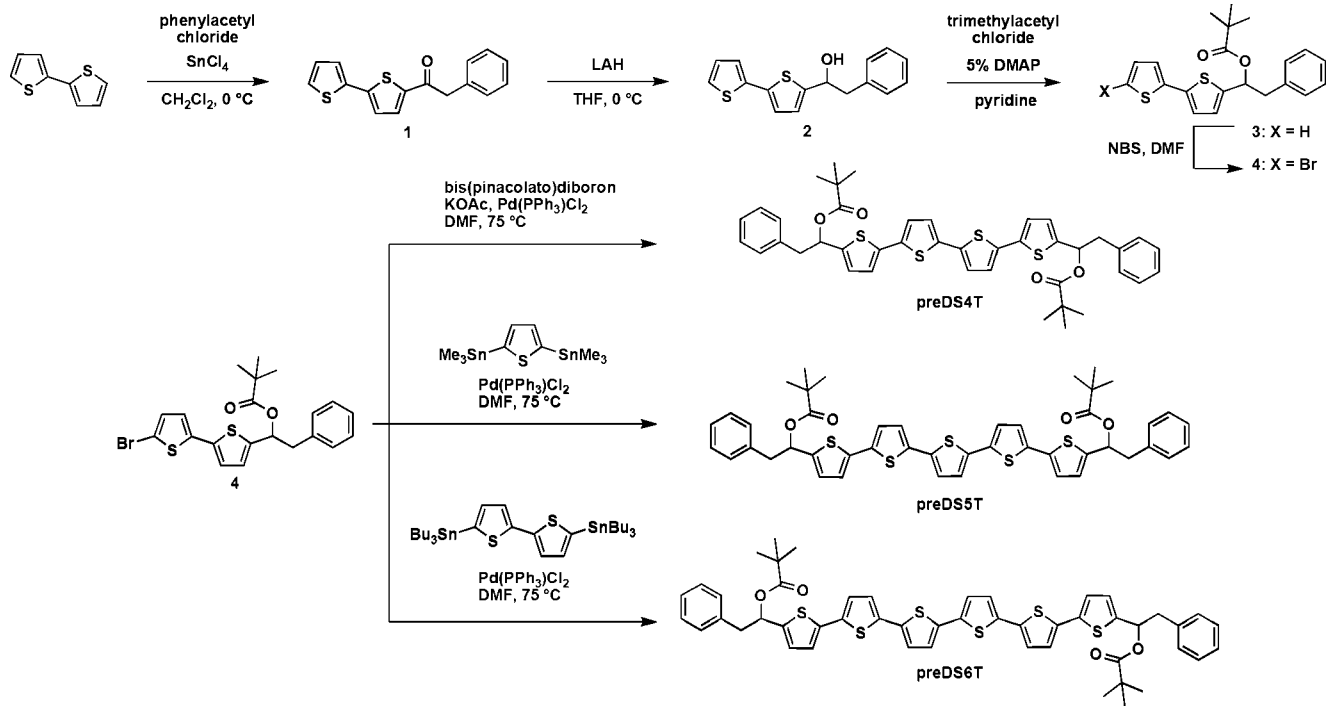

removal of ester solubilizing groups without further degradation of the material.

UV−Vis and MALDI-TOF Characterization. UV−vis absorption spectra of the precursor oligomers (**preDS4T**, **preDS5T**, and **preDS6T**) exhibit characteristic absorption patterns of the oligothiophene cores (see the Supporting Information). Peak absorbance values within the series of oligothiophenes increase with conjugation length: 400 nm for **preDS4T**, 424 nm for **preDS5T**, and 436 nm for **preDS6T**. Conversion of **preDS4T** to **DS4T** results in a red-shift of 40 nm, as shown in Figure 3, and the wavelength of maximum absorption corresponds to that of **DS4T** prepared via an alternate route.[9]

Analysis of the thermally prepared **DS4T** by MALDI-TOF mass spectrometry reveals a single signal that corresponds to the mass of **DS4T** (see the Supporting Information). Higher mass signals that would result from polymerization of the styryl groups were not observed. This data, representative of all derivatives, suggests that our original design involving the thermal conversion of the precursor oligomers to α,ω-distyryl oligothiophenes is indeed valid. However, the practical application of this approach to prepare semiconducting films depends critically on the morphology of the resulting films.

Film Morphology and Structural Characterization. Using a previously developed procedure,[24] we spun-cast films of each precursor oligomer from 2−3 mg/mL solutions in chloroform onto freshly oxidized silicon wafers with 100 nm of thermally grown oxide. The substrates were thermally annealed under nitrogen at 200−225 °C for 20 min to convert the precursor oligomers into α,ω-distyryl oligothiophenes. The morphology of the ultrathin films was examined using AFM and a detailed structural characterization of the molecular packing and alignment was conducted using NEXAFS spectroscopy and GIXD.

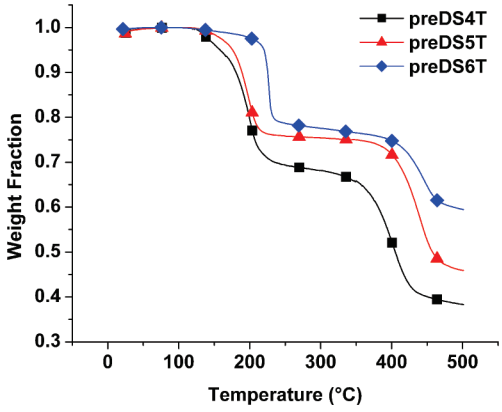

Figure 2. Thermogravimetric analysis conducted at 5 °C/min. Thermolysis of esters results in an expected weight loss of 28% for **preDS4T**, 25% for **preDS5T**, and 23% for **preDS4T**.

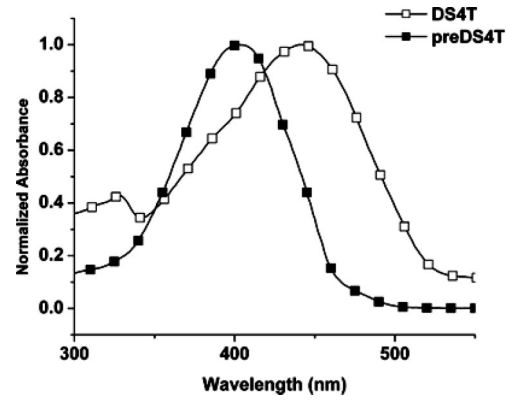

Figure 3. Thermal conversion of **preDS4T** to **DS4T** results in a red-shift of 40 nm and a loss of solubility. Additional peaks in the absorption spectrum of **DS4T** are likely associated with the phenyl end groups.

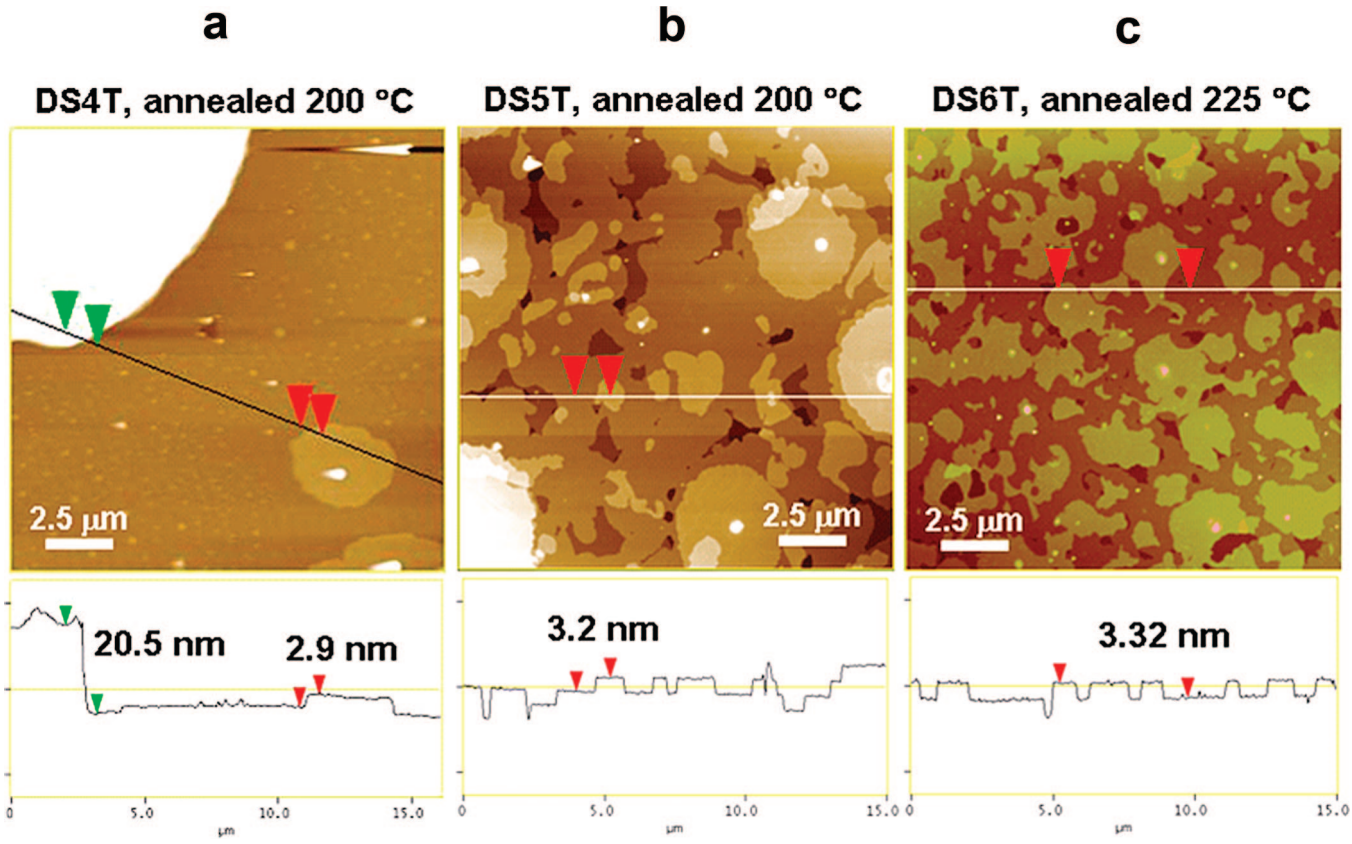

Figure 4. AFM images of thermally treated films of **DS4T** (a), **DS5T** (b), and **DS6T** (c). Island formation is suppressed and layer growth encouraged by lengthening the oligothiophene backbone, as seen in (a), (b), and (c).

AFM reveals that films of **DS4T** exhibit poor surface coverage after thermal conversion as shown in Figure 5a. The majority of the surface shown appears bare and only isolated islands are seen with most of the material clumped into large islands, such as the one shown in the upper left of the image. This finding is supported further by the following NEXAFS data (vide infra), and is consistent with previous studies involving oligothiophenes with thermally labile solubilizing groups in which quarterthiophene films failed to maintain surface coverage after thermal annealing.[21] In that work, increasing the length of oligothiophene cores of thermal precursors from 4T to 7T allowed films to be treated at progressively higher temperatures to yield continuous films. The temperature required for ester thermolysis imparts enough energy for **DS4T** to overcome the substrate surface energy and form islands. In contrast, thermal conversion of the precursor oligomers of **DS5T** and **DS6T** generates thin films with excellent surface coverage and a terraced multilayer morphology, which is characteristic of highly ordered films, as seen in images b and c in Figure 4. A trend of increasing step heights consistent with the lengths of the molecules is observed, which suggests that the films are composed of stacked monolayers of nearly vertically aligned oligomers. Note that in both cases the resulting films are only a few nanometers thick.

A systematic shift in the morphology of the three films is observed from a predominantly island growth mode to a more layer-island growth mode.[25,26] Although **DS4T** shows a strong tendency for island growth only, **DS5T** appears to form a couple of continuous layers before additional layers grow as islands. In contrast, films of **DS6T** show an even stronger tendency for a layer-by-layer growth. However, both the **DS5T** and **DS6T** form continuous films as seen in the following X-ray diffraction and NEXAFS data. Because film continuity is essential for the fabrication of the OFETs, only the **DS5T** and **DS6T** films are of interest for structural and electrical characterization.

NEXAFS Spectroscopy. We have previously shown that NEXAFS spectroscopy can be an effective tool to study the conversion, orientation, and surface coverage of solution-processed organic semiconductors formed by a thermolysis strategy.[27,28] A series of films of each oligomer (**DS4T**, **DS5T**, and **DS6T**) were prepared for NEXAFS analysis by spin-casting and thermal treatment up to 250 °C followed by quenching to room temperature. NEXAFS spectroscopy is based on the resonant excitation of core electrons—which for low-z elements are in the K shell— to unfilled molecular orbitals, which are typically of antibonding character. The technique is therefore element-specific by selection of the soft X-ray energy range to match a particular core shell and bond-specific by the energy of the final state accessed.[29] Both

(24) Chang, P. C.; Lee, J.; Huang, D.; Subramanian, V.; Murphy, A. R.; Fréchet, J. M. J. *Chem. Mater.* **2004**, *16*, 4783–4789.
(25) Bauer, E. *Z. Kristallogr.* **1958**, 372.
(26) Muller, E.; Ziegler, C. *J. Mater. Chem. 10* **2000**, 47–53.
(27) DeLongchamp, D. M.; Sambasivan, S. *Adv. Mater.* **2005**, *17*, 2340–2344.
(28) DeLongchamp, D. M.; Jung, Y.; Fischer, D. A.; Lin, E. K.; Chang, P.; Subramanian, V.; Murphy, A. R.; Fréchet, J. M. J. *J. Phys. Chem. B* **2006**, *110*, 10645–10650.
(29) Stöhr, J. *NEXAFS Spectroscopy*; Springer-Verlag: Berlin, 1992; Vol. 392.

carbon K-edge and oxygen K-edge NEXAFS spectra reveal details of the transformation from **preDSnT** to **DSnT**. The carbon edge spectra reveal the chemical transformation of the material as well as the molecular orientation, whereas the oxygen edge spectra reveal chemistry associated with carbonyl removal as well as coverage via the exposure of the underlying silicon oxide substrate.

The carbon K-edge NEXAFS spectra shown in Figure 5 follow the chemical conversion of the **preDS5T** to **DS5T**. Conversion is most readily observed by changes in the position of the carbon−carbon 1s → π^* resonance near 285 eV and the carbonyl 1s → π^* resonance near 288.5 eV; the intensity of the carbon−hydrogen 1s → σ^* resonance at ∼287.4 eV changes with the amount of carbon−hydrogen bonds relative to the overall carbon content. The **preDS5T** film as-cast and after heat treatment to 100 °C exhibits a narrow C═C π^* peak located at 285.3 eV. After the film is exposed to temperatures of 150 °C and above, the peak location shifts to 285.0 eV and the peak broadens substantially. This change in C═C π^* character can be related to the conversion of **preDS5T** to **DS5T**. The styryl group resulting from the thermolysis process adds an alkenyl carbon−carbon double bond to the core 5T molecule extending its conjugation. The newly formed alkene bond is not part of a ring and is expected to have a somewhat greater length than the other π bonds. Because longer π^* bonds typically exhibit lower-energy NEXAFS resonances, the shift in the C═C π^* peak location after exposure to temperatures >150 °C can be attributed to the convolution of the lower-energy alkene resonance with the aromatic resonances of the core 5T. It is of course possible that changes in the other bonds due to resonance could also shift the peak character. Because of energy resolution limitations and the expected peak broadening that occurs in solid state samples, we cannot discriminate the individual resonances. The C═C π^* peak shape and location are nominally identical for exposure to 150 °C and above. These data therefore show that **preDS5T** is converted to **DS5T** between 100 and 150 °C. By a similar analysis, **preDS4T** was found to convert between 100 °C and 150°, whereas **preDS6T** was found to convert between 150 and 200 °C.

Altough the C═C π^* trend indicates that conversion is completed by 150 °C, the carbonyl π^* trend reveals that the pivalic acid is not removed until the film is exposed to much higher temperatures. In the **preDS5T** film as-cast and after heat treatment to 100 °C, the carbonyl π^* peak is located at ∼288.7 eV. After the film is exposed to temperatures of 150 and 200 °C, the carbonyl peak location shifts to 288.3 eV. Because the C═C π^* trend indicates that the conversion is completed by 150 °C, it is reasonable to attribute this shift in carbonyl character to the conversion of the ester to pivalate. The molar density of pivalate carbonyl present at 150 °C appears to be on the same order as the precursor carbonyl density. The intensity of the pivalate π^* peak is significantly decreased by 200 °C, but it is removed only after heating to 250 °C. We note that these NEXAFS spectra were collected in partial electron yield (PEY) mode at a grid bias of −50 V, so that the spectra reflect the chemistry within ∼4 nm of the top surface of the film. We therefore cannot determine whether the residual pivalic acid is evenly distributed throughout the film or only present at the top interface. However, it is clear that significant residual pivalic acid is present in films exposed to temperatures below 250 °C.

NEXAFS spectroscopy can also be employed to follow changes in molecular orientation throughout the conversion process. The substrate-relative orientation of molecular resonances can be determined by changing the orientation of the electric field vector with respect to the substrate, which is typically accomplished by changing the angle of beam incidence. Spectra of **preDS5T** and **DS5T** are shown in spectra a and b in Figure 6. The variation in C═C π^* intensity with incident angle reveals strong molecular orientations relative to the substrate both before and after conversion. In **preDS5T**, the intensity of the C═C π^* resonance is greatest at 20° incidence, where the electric field vector is tilted 20° away from surface normal, indicating that the molecular π^* vector is preferentially tilted away from the substrate plane. In contrast, **DS5T** has the greatest C═C π^* intensity where the electric field vector is tilted >80° away from surface normal, indicating that the π^* vector is preferentially tilted parallel to the substrate plane.

The orientation of the π^* vector with respect to the molecule can be understood from the illustration shown in Figure 6d. A π^* resonance has a transition dipole that is perpendicular to a double bond; in ring systems, the sum of the π^* resonances is a vector perpendicular to the ring plane. In **DS5T**, and all α,ω-distyryl oligothiophenes for which the rings are expected to be coplanar, the molecule is expected to exhibit a single π^* orientation normal to the coplanar rings. Because the **preDS5T** π^* vector is preferentially aligned away from the substrate plane, the substrate plane and the molecular conjugated plane are more parallel in a "plane on" arrangement. In contrast, the **DS5T** π^* vector is preferentially aligned parallel to the substrate plane, so the substrate plane and molecular conjugated plane are more perpendicular in a preferentially "edge on" arrangement. We previously observed a qualitatively similar precursor/product orientation shift in thin films of thermally convertible thiophene semiconductors with pendant alkylene substitution rather than styrene substitution.[27,28]

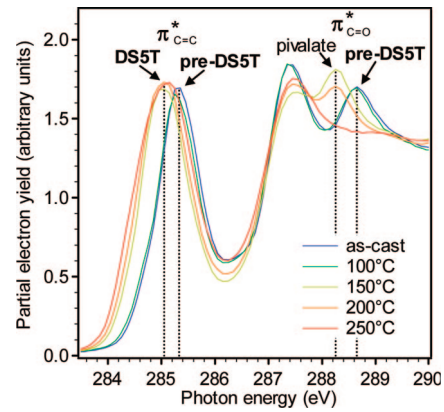

Figure 5. NEXAFS carbon K-edge spectra following the conversion of the **preDS5T** to **DS5T**.

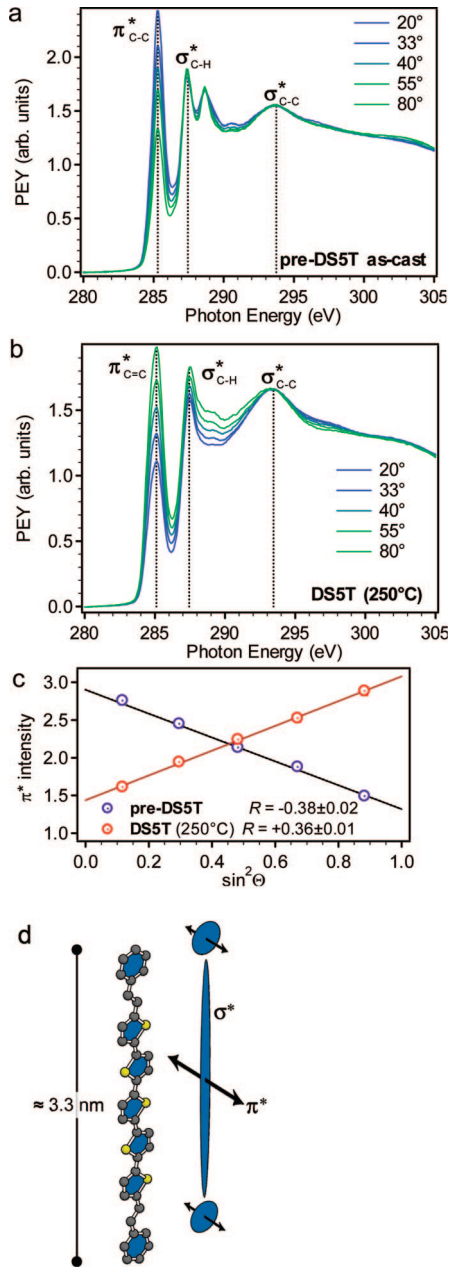

Figure 6. Orientation analysis of **preDS5T** and **DS5T**, including spectra of (a) **preDS5T** and (b) **DS5T** (250 °C) each collected at 5 incident angles, (c) fits of the C=C π^* intensity to incident angle, and (d) an illustration of the primary π^* and σ^* resonance orientations for **DS5T**.

Although the π^* vector orientation describes the orientation of the molecular conjugated plane, it does not describe the orientation of the molecular long axis. The AFM images shown previously suggest a roughly vertical long axis orientation for the converted **DS5T**, based on the similarity of layer thickness to long axis length, as does the X-ray diffraction (vide infra). This vertical long axis orientation is consistent with the edge-on **DS5T** conjugated plane. A vertical long axis orientation is further supported by the NEXAFS carbon−hydrogen σ^* resonance orientation of **DS5T**, which is roughly parallel to the surface plane, because σ^* transitions are parallel to the bond, and the net carbon−hydrogen bond orientation of **DS5T** is more perpendicular to the long axis than it is parallel. The vertical long axis orientation is also supported by the slight vertical

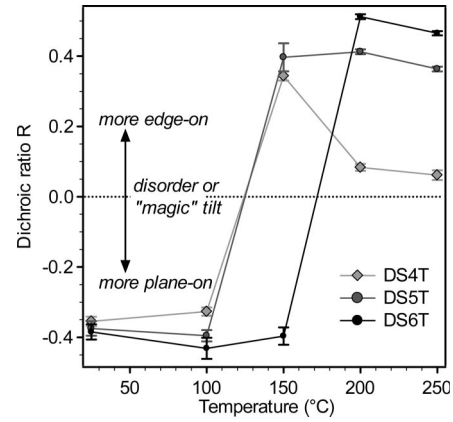

Figure 7. Changes in molecular orientation over the conversion of **pre-DSnT** to **DSnT**.

preference of the carbon−carbon σ^* resonance at ~298 eV, because the carbon−carbon bonds are more parallel to the long axis than perpendicular to it. Although these two resonance trends support the vertical long axis assignment, we note that neither provides sufficient information to quantify the long axis orientation.

The π^* vector orientation can be quantified using a dichroic ratio, R, which we have previously defined.[27,28] The quantity R varies from −1.0 for a perfect plane-on orientation such as that exhibited by highly oriented pyrolytic graphite, to 0.7 for a perfectly edge-on orientation. An R value of 0, which occurs when the resonance intensity does not vary with incident angle, indicates either an isotropic system or one in which the resonance is tilted 54.7° (the "magic angle") away from surface normal. The R-values are determined by a simultaneous fit of π^* intensity to the squared sine of incident angle, as shown in Figure 6c. The quantified plane-on and edge-on preferences of **preDS5T** ($R = -0.38$) and **DS5T** ($R = 0.36$), respectively, are significant (e.g., far from $R = 0$), but not absolute (e.g., not −1.0 and not 0.7, respectively). If the samples were well-described by a single π^* vector orientation, the π^* vector of **preDS5T** would tilt ~41° from surface normal while that of **DS5T** would tilt ~67°. However, this assumption is likely to be incorrect as we believe that the π^* orientation distribution is broadened by molecular disorder and may also be bimodal if the molecules are in a herringbone-packed, two-molecule unit cell (as suggested by the GIXD) with inequivalent surface-relative molecular tilts. The average π^* vector tilt provides important constrains on possible long axis orientations. The average **preDS5T** long axis tilt from substrate normal cannot be less than 90° − 41° = 49°, whereas the average **DS5T** long axis tilt cannot be less than 90° − 67° =23°.

Changes in molecular orientation throughout the conversion from **pre-DSnT** to **DSnT** may be followed by the π^* vector R of samples exposed to heat treatment, as shown in Figure 7. All three precursors exhibit plane-on orientation until full chemical conversion is achieved, which occurs above 100 °C for **preDS4T** and **preDS5T**, and above 150 °C for **preDS6T**. After conversion, all molecules exhibit an edge-on orientation preference. Notably, the presence of excess pivalate does not appear to disturb or alter the molecular orientation. The greatest edge-on preference is

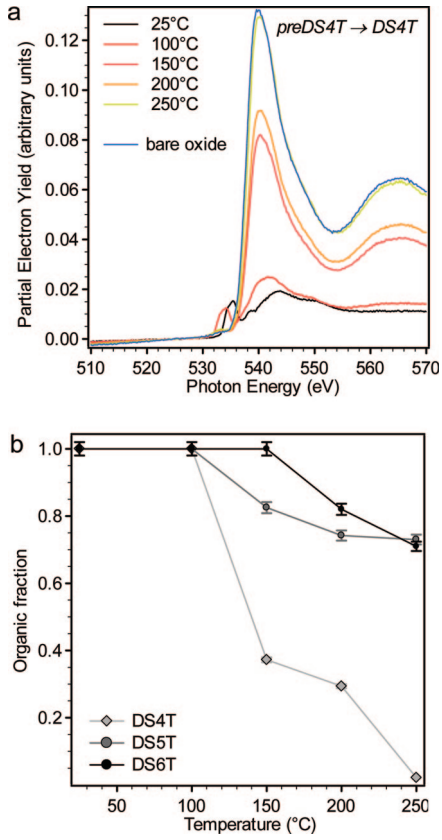

Figure 8. (a) NEXAFS data for a thermally prepared **DS4T** film. Above 100 °C, the spectrum rapidly approaches that of bare silicon oxide. (b) Organic fraction coverage trend for the three precursors.

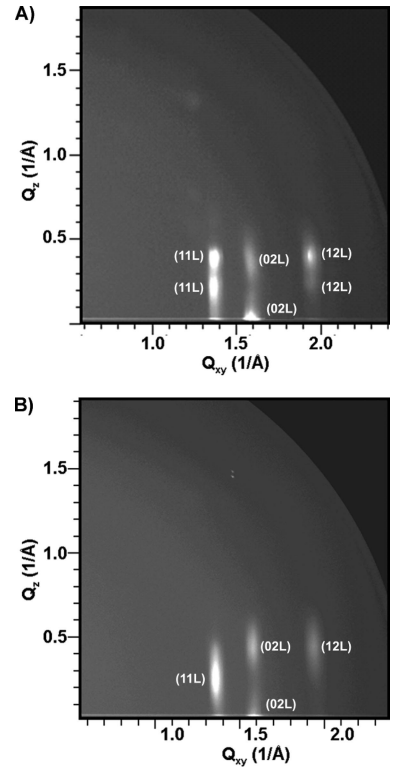

Figure 9. Grazing incidence X-ray diffraction (GIXD) areal plots of (A) **DS5T** and (B) **DS6T**, respectively, showing the different peaks in Q_{xy} and Q_z directions. The Q_{xy} and Q_z values are accurate to approximately 0.005 and 0.01 $Å^{-1}$, respectively.

exhibited by **DS6T** at 200 °C. At temperatures exceeding that required for conversion, the edge-on orientation appears to decrease. This effect is most significant for **DS4T**, which loses most of its orientation preference above 150 °C, with a trend toward the disorder condition ($R = 0$). We believe that this loss of orientation is related to a reduction in surface coverage (i.e., formation of more islands), leading to poor intermolecular packing and substantial disorder. More modest losses of edge-on orientation are observed for both **DS5T** and **DS6T** at 250 °C.

The loss in surface coverage at higher temperatures is supported by oxygen K-edge NEXAFS data showing an increase in the contribution of the underlying silicon oxide substrate as temperature increases. Because the partial electron yield signal is surface-sensitive, the increasing substrate contribution can only be attributed to thinning or discontinuity in the organic layer. The series of NEXAFS spectra shown in Figure 8a illustrate the loss of surface coverage for **DS4T**. Above 100 °C, the spectrum shape and intensity rapidly approaches that of silicon oxide. This loss in coverage is consistent with our AFM observations showing that the films rapidly lose surface coverage at temperatures greater than 100 °C. The organic fraction can be quantified by the fraction of the spectrum which does not resemble silicon oxide, as shown in Figure 8b. The **DS5T** and **DS6T** films exhibit greater persistence of film surface coverage at higher temperatures.

GIXD Analysis. Although NEXAFS spectroscopy is an excellent technique for monitoring the chemical and morphological changes that take place during thermal treatment of films, it does not provide information on the film crystallinity or on the detailed crystal structure. This can be obtained from X-ray diffraction, but to date, an explicit diffraction study of the crystallinity of these films has not been performed. An analysis of the packing mode of the oligothiophenes and the degree of crystallinity in these films is valuable, as it would provide a comparison of the crystal structure of thermally converted oligothiophene films to films grown via vapor-deposition. Therefore, we used both synchrotron-based X-ray diffraction and NEXAFS spectroscopy to elucidate the structure and molecular packing of these ultrathin films.

The in-plane and out-of-plane crystalline order in the films was probed with GIXD (small incidence angles) and specular diffraction, respectively. For the GIXD experiments, the substrates are Si wafer pieces with a 10 nm thick SiO_2 film. Panels a and b in Figure 9 show the grazing incidence X-ray diffraction data obtained on a 2D image plate, which records intensity (I) as a function of q_{xy}, q_z, which are the in-plane and out-of-plane components of the scattering vector, respectively. Individual peak positions, shown in Table 1, are obtained after an appropriate background correction and Gaussian fits to the data.[30] As the AFM data show, these films consist of a continuous monolayer in contact with the substrate and discontinuous layers atop this monolayer. This heterogeneous morphology makes it nearly impossible to quantitatively analyze the film structure. The diffraction from

(30) Merlo, J. A.; Newman, C. R.; Gerlach, C. P.; Kelley, T. W.; Muyres, D. V.; Fritz, S. E.; Toney, M. F.; Frisbie, C. D. *J. Am. Chem. Soc.* **2005**, *127*, 3997–4009.

Table 1. Peak Positions in the GIXD Data

peak	Q_{xy} (Å^{-1})	Q_z (Å^{-1})
	DS5T	
(11 L)	1.362	0.18
(11 L)		0.40
(02 L)	1.579	0
(02 L)		0.39
(12 L)	1.931	0.23
(12 L)		0.40
	DS6T	
(11 L)	1.360	0.18
(02 L)	1.580	0
(02 L)		0.44
(12 L)	1.928	0.44

a monolayer consists of Bragg rods, diffraction that is sharp along of q_{xy} but extended along q_z, whereas that from a 3D crystal has Bragg spots, sharp along both q_{xy} and q_z. For a multilayer, the diffraction is intermediate between these as there is interference between the diffraction from each layer leading to a modulation in the intensity of the Bragg rods. The diffraction from these films consists of all above and hence we cannot unambiguously index the q_z components of the spots/rods, although we accurately determine the in-plane lattice. Hence, in the discussion that follows we label the peaks as (*hkL*), where *hk* are determined, but *L* is not identified.

The absence of (10*L*) and (01*L*) peaks/rods shows the molecules adopt a herringbone edge-to-face packing, which is commonly observed in oligothiophene molecules. The in-plane lattice parameters *a*, *b*, and γ are calculated using the q_{xy} positions of the peaks. For the **DS5T** system, the peaks are indexed to a rectangular unit-cell with dimensions $a = 5.659 \pm 0.005$ Å, $b = 7.955 \pm 0.005$ Å, and $\gamma = 90°$. Given the similar molecular structure for the two systems it is not surprising that the **DS6T** systems also shows a rectangular unit-cell with dimensions almost identical to **DS5T** systems; $a = 5.675 \pm 0.005$ Å, $b = 7.957 \pm 0.005$ Å, and $\gamma = 90°$. In principle, the q_{xy} and q_z data from GIXD can be used to determine the 3D lattice parameters of the thin film unit cell.[30,31] However, as mentioned above, the poorly defined morphology obviates such an analysis. The rationale for using such ultrafilms for the GIXD analysis was to study the crystallinity in the films with the same morphology as that in the OFETs. These GIXD experiments show that there is good in-plane crystallinity in such films.

In addition to the GIXD data, specular X-ray diffraction measurements of these ultrathin films can be used to estimate the interlayer spacing for both of the films. This data shows fairly weak peaks due to the ultrathin nature of the films, which are only ~2−4 layers thick, with not more than two continuous layers. Nonetheless, we were able to model the data in both cases, as shown in Figure 10.

A reasonable fit to the **DS5T** film data is obtained by modeling the film as consisting of up to 4 layers with decreasing coverage for successive layers. Specifically, first layer, 100% coverage and thickness of 4 nm; second layer, 83% coverage and thickness of 3.65 nm; third layer, 33% coverage and thickness of 3.6 nm; fourth layer, 6% coverage

(31) Fritz, S. PhD Dissertation, University of Minnesota, Twin Cities, MN, 2007.

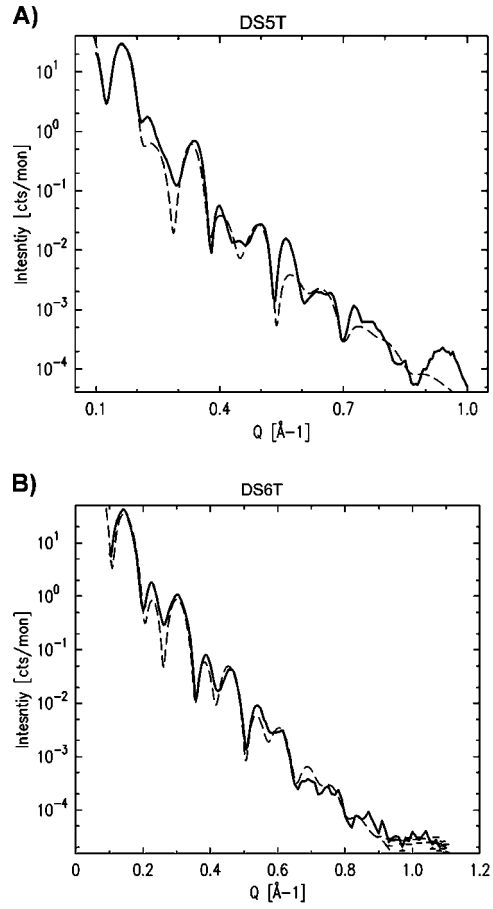

Figure 10. Specular measurements on (A) **DST5** and (B)**DST6** films, respectively, with morphology similar to that in the AFM images in Figure 5. The dashed lines show the model fit to the raw data.

and thickness of 3.6 nm. Using these parameters, we calculated the average interlayer spacing to be $d = 3.8$ nm. Note that the layer closest to the SiO_2 is thicker than the other three layers. Similarly, a model fit to the **DST6** film data is obtained by modeling only 2 layers with decreasing coverage for successive layers. (i.e., first layer, 100% coverage and thickness of 4.25 nm; second layer, 60% coverage and thickness of 3.95 nm.) Using this model, we then calculated the average interlayer spacing to be $d = 4.14$ nm, and a decrease in thickness for the second layer is also noted. The choice of the number of layers as well coverage of each layer is validated by looking at the AFM images of the films. Using DFT calculations, the molecular lengths for the **DS5T** and **DS6T** are estimated to be 32.7 and 37.0 Å, respectively. (This is the H−H distance measured from the 4-position hydrogen nuclei on the terminal phenyl groups.) At this time, we are unable to explain the variation in layer thickness definitively. We hypothesize that the larger thickness of the first layer located next to the SiO_2 surface results from the presence of some adventitiously adsorbed hydrocarbons or water (a few Angstroms) on the SiO_2. Furthermore, the decrease in the interlayer spacing with increasing thickness may be due to some material that remains within the successive layers after the thermolysis process. Given that the NEXAFS data show trace amounts of pivalic acid byproduct present in the films after thermolysis, it is possible that this impurity affects the layer thickness. It is also likely

Table 2. Average Saturation Mobilities and on/off Ratios for a Set of Six Devices

	μ (cm^2/(V s))	on/off
DS5T	0.051 ± 0.007	1×10^6
DS6T	0.043 ± 0.006	1×10^5

that substrate effects dominate the crystallization of the bottom layers so that the ultrathin films do not grow in a layer-by-layer fashion.[31]

These diffraction data, the first obtained for an ultrathin thermolysis based oligothiophene film, demonstrate that the same intermolecular packing observed in vapor deposited films is preserved in these solution deposited films. The presence of good in-plane crystallinity, critical for charge transport in OFET device geometry, shows that the thermolysis process, which has been introduced to allow solution deposition, does not compromise the eventual quality of the organic semiconductor thin films. More importantly, the intermolecular packing of **DS5T** and **DS6T** in the present study is consistent so that any differences in air stability observed for the materials result from structural variations at the molecular level.

Electrical Characterization. OFET devices were fabricated on low resistivity n-type silicon wafers, using 1000 Å of thermally grown SiO_2 as the dielectric, in top contact geometry. The active semiconducting layer was applied by spin-casting 2−3 mg/mL solutions of the oligomers in chloroform, and the films were then annealed at 200 °C for **DS5T** and 225 °C for **DS6T** in a nitrogen atmosphere. Gold contacts were patterned on top of the films using various shadow masks giving channel lengths from (5 to 40) μm and widths from (200 to 400) μm. All devices were tested as p-type OFETs in the accumulation regime and saturation mobilities were calculated using the equation, $\mu = g_m^2/2I_DC_{ox}(W/L)$, where g_m = transconductance, I_D = current measured at the drain electrode, C_{ox} = capacitance of the insulator, W = width of the electrodes, and L = channel length.

Functional OFETs were obtained for thermally converted films of **DS5T** and **DS6T**, but not for **DS4T** because of its poor film morphology as discussed above. Devices fabricated with **DS5T** and **DS6T** were initially tested under nitrogen to minimize the effects of oxygen. The average mobility values and on/off ratios for a set of six devices are summarized in Table 2. Representative output and transfer *IV* curves are shown in Figure 11 for **DS5T** and Figure 12 for **DS6T**.

Short-Term Air Exposure. To monitor the short-term effects of exposure to ambient conditions on the electrical properties of **DS5T** and **DS6T**, we prepared films on patterned silicon substrates to yield bottom contact OFETs with W = 500 μm and L = 20 μm. The substrates were placed inside a custom-built automated probe station capable of testing four devices simultaneously. The devices were then tested in the dark under ambient conditions once every hour for 3 days. To derive threshold voltage and mobility values from I_D, the devices were biased at $V_D = -20$ V with a short V_G sweep from (−17 to −20) V. The saturation current and mobility measured for each device is plotted as a function of time in Figure 13.

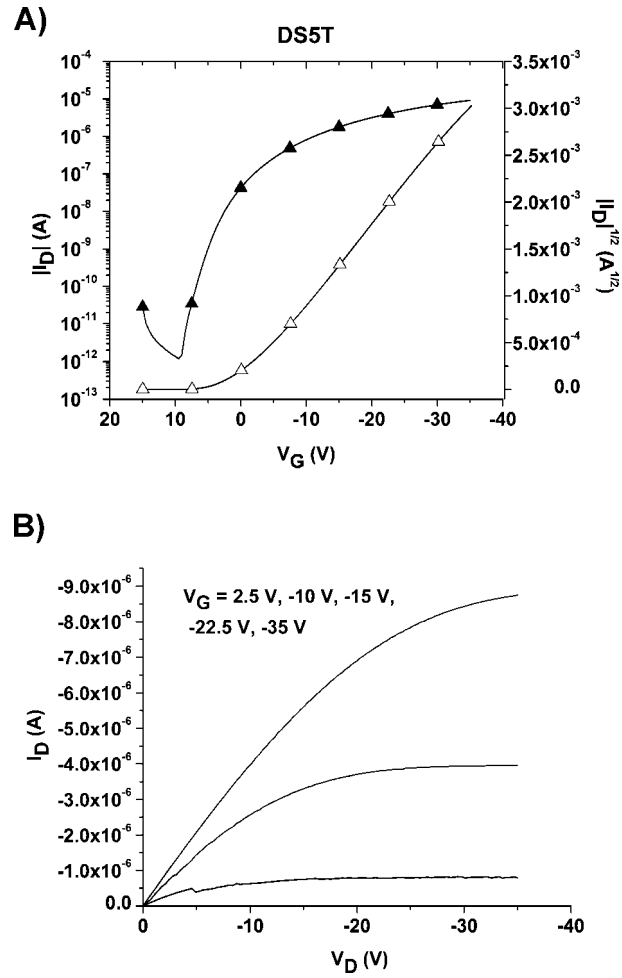

Figure 11. (A) Transfer and (B) output *IV* plots for a top-contact **DS5T** device with W = 400 μm and L = 40 μm. The current levels measured at V_G = (2.5 and −10) V are too low to distinguish in the plot.

The data show different behavior for **DS5T** and **DS6T** initially, but both sets of devices exhibit a stabilization in I_D after the first day of testing. The calculated mobility values are an order of magnitude lower than those values obtained in top-contact devices, which is likely the result of poor contacts with the patterned electrodes and the relatively lower V_G and V_D values accessible in the automated probe station. For each device, the evolution of saturation mobility tracks the trend seen in I_D. The saturation current shows a significant increase upon exposure to air for both **DS5T** devices, whereas both **DS6T** devices exhibit a slight decrease in current. This effect is the result of V_T shifting to negative values for **DS6T** devices while remaining close to zero for **DS5T** devices (see the Supporting Information). Neither set of devices show a trend of decreasing mobility over the trial period.

Long-Term Device Testing. To track the effect of ambient conditions on the performance of **DS5T** and **DS6T**, top-contact device substrates were stored in air protected from light and the transistor performance was tested periodically. Long-term testing of the devices revealed that both **DS5T** and **DS6T** are highly resistant to degradation due to ambient conditions for at least 130 days. Saturation mobilities measured for **DS5T** and **DS6T** as a function of days stored in air are shown in Figure 14.

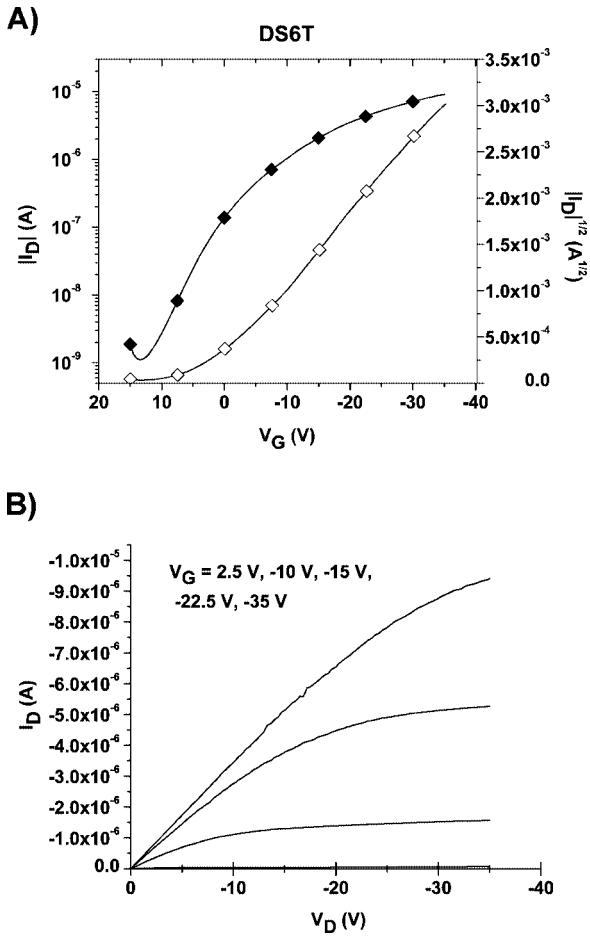

Figure 12. (A) Transfer and(B) output *IV* plots for a top-contact **DS6T** device with $W = 400$ μm and $L = 40$ μm.

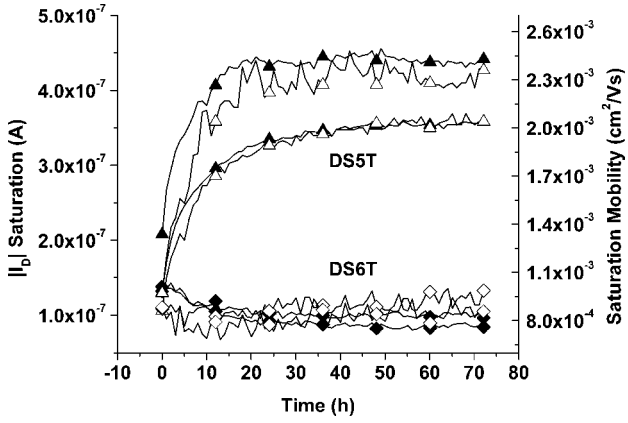

Figure 13. Short-term evolution of device performance for a set of four bottom-contact devices as a function of hours exposed to air. Trends in I_D (solid symbols) match trends in μ (outlined symbols).

High on/off ratios were initially obtained as mentioned previously and maintained over the time period shown in Figure 14 through the application of positive gate bias. This characteristic of the devices is probably due to the oxidative doping of **DS5T** and **DS6T** as a result of exposure to atmospheric oxygen. Because initial testing of the devices revealed a positive turn-on voltage, it is likely that **DS5T** and **DS6T** rapidly dope even upon slight exposure to oxygen. This characteristic of the materials is not surprising given that the oligomers contain no

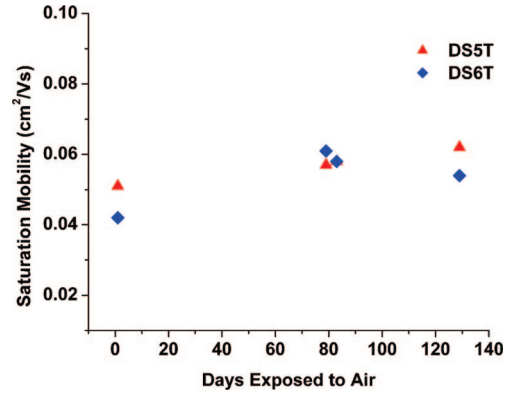

Figure 14. Plot of μ as a function of days stored in air for a pair of top-contact devices. The variation in the observed μ correlates with the variation observed in initial device testing (Table 2). No trend toward lower saturation currents is observed.

electron-withdrawing substituents, which are known to render materials resistant to oxidative doping. However, both materials seem to rapidly reach a stable level of doping that does not result in oxidative degradation of the material, as evidenced by the high mobility values maintained over the entire period of the study (see Figure 14). This is important, because the resulting devices therefore have predictable and well-controlled threshold voltage levels and on−off ratios. Furthermore, devices utilizing **DST5** and **DST6** still provide high saturation currents and low off currents even after storage in air for 130 days, as shown in panels A and B in Figure 15, respectively.

Discussion

Structural analysis of **DS4T**, **DS5T**, and **DS6T** films by AFM reveals a trend of island growth evolving into a more layer-by-layer growth mode as the oligothiophene backbone is lengthened. As a result, **DS4T** fails to form a continuous film and a direct comparison between ultrathin films deposited using our methods and previously published vapor-deposited films is impossible.[9] Fortunately, **DS5T** and **DS6T** both formed continuous films that exhibit high levels of surface molecular orientation in NEXAFS and high levels of crystallinity in GIXD.

Previous studies on oligothiophenes with thermally labile solubilizing groups demonstrated the tendency of these materials to orient on silicon oxide surfaces and showed a monolayer provided ideal electrostatics in OFET channels.[32] Given the GIXD data presented here, this result can be rationalized to arise from the lack of layer-by-layer growth in the crystalline films. Each layer boundary may then exist as a probable site for impurities and charge traps. Because of the ultrathin nature of the films, neither **DS5T** nor **DS6T** transition into a bulk 3D crystalline phase. In fact, only the very bottom layer of either oligomer is completely continuous and therefore conducts the majority of charge in OFET channels. Nevertheless, GIXD data shows that edge-to-face

(32) Chang, P.; Molesa, S. E.; Murphy, A. R.; Fréchet, J. M. J.; Subramanian, V. *62nd Device Research Conference Digest*; IEEE: Piscataway, NJ, 2004; Vol. 1, p 183.

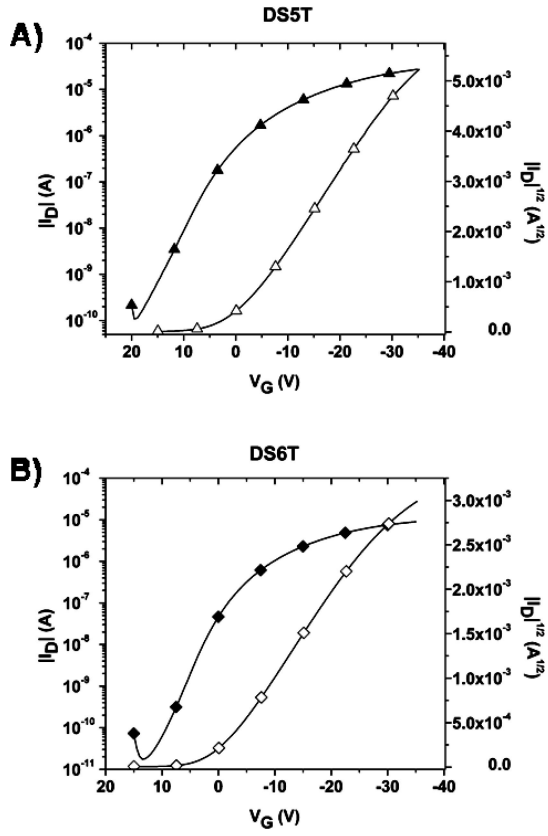

Figure 15. (A) **DS5T** transistor after storage in air for 130 days, device dimensions $L = 20$, $W = 400$. (B) **DS6T** transistor after storage in air for 130 days, device dimensions $L = 20$, $W = 200$.

intermolecular packing, predominant in vapor-deposited organic semiconductor films,[33−35] is preserved in solution processed films of **DS5T** and **DS6T** after thermal annealing.

A direct consequence of the ultrathin nature of these films is that no barrier exists between the active layer of **DS5T** or **DS6T** and atmospheric oxygen. Therefore, tracking the performance of **DS5T** and **DS6T** in OFETs exposed to air provides a sensitive probe of the stability of the materials toward oxidative degradation. In a 72 h trial of bottom-contact devices, neither **DS5T** nor **DS6T** showed signs of degradation in terms of hole mobility. Instead, **DS5T** exhibited an increase in hole mobility and the threshold voltage of **DS6T** devices shifted to negative values. Both sets of devices displayed stable operation after 24 h. The difference in the behavior of **DS5T** and **DS6T** in this experiment is not easily rationalized, as the two oligomers provide more consistent performance in top-contact devices. It may be that the transitional phase of the device performance that was observed by testing the bottom-contact devices once every hour went unnoticed in the long-term testing of top-contact OFETs. However, both **DS5T** and **DS6T** OFETs fabricated in top-contact geometry always displayed slightly positive threshold voltages. This characteristic suggests that top-contact OFET geometry reduces the population of trap-states at the metal-semiconductor interface for these materials, although the reason why only **DS6T** in bottom-contact OFETs exhibits a threshold voltage shift is not clear.

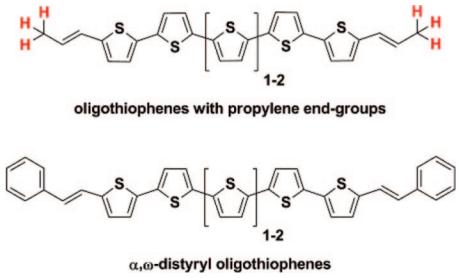

Figure 16. Effect of end-group structure on stability is likely tied to the presence of moieties susceptible to auto-oxidation.

In top-contact devices, **DS5T** and **DS6T** have, respectively, hole mobilities of 0.05 and 0.04 $cm^2/(V\ s)$ and on/off ratios greater than 1×10^5. These values remained virtually unchanged over the course of 130 days of storage in air. These stability tests were conducted in the dark to allow a comparison to published stability data for oligothiophenes.[9,20] The stability of these devices implies that the structures of the molecules are especially resistant to the irreversible oxidation reactions that lead to a loss of conductivity in OFET channels. For example, the mobility of octathiophene (8T) in OFETs exposed to air is known to decrease by 70% after 100 days.[9] Oligothiophenes are known to be reactive at the α-carbon of the terminal thiophene rings, especially in the oxidized state.[36] This may render unsubstituted oligothiophene OFETs relatively unstable to operation in air. In a previous study with oligothiophene films prepared via thermolysis of ester solubilizing groups, a decrease of 20% was reported to occur in a shelf life test of 1 week and long-term sustainability of high mobility was not observed.[20] Those oligothiophenes were substituted with propylene end-groups and differ from α,ω-distyryl oligothiophenes studied here only in the replacement of a methyl for a phenyl group, as shown in Figure 16.

The conspicuous structural difference between these molecules is the presence of allylic carbon−hydrogen bonds in the propylene end groups and the absence of any correspondingly weak bonds in the styryl end groups. Given the well-known susceptibility of electron-rich olefins to oxidation at the allylic position,[37] the oxidative modification of oligothiophenes with propylene end groups likely proceeds via this pathway.

Because styryl end groups have a stabilizing effect on quaterthiophene, pentathiophene, and sexithiophene, the originally reported stability of **DS4T** is likely not a special property of that conjugated molecule but instead appears to be an end-group effect. This effect appears to arise from the ability of styryl end groups to block the reactive sites in oligothiophenes without introducing structures susceptible to auto-oxidation.

(33) Yuan, Q.; Mannsfeld, S.C. B.; Lüning, J; Tang, M.; Roberts, M.; Toney, M. F.; DeLongchamp, D. M.; Bao, Z. *Chem. Mater.* **2008**, *20*, 2763–2772.
(34) Yuan, Q.; Mannsfeld, S.C. B.; Tang, M.; Toney, M. F.; Lüning, J.; Bao, Z. *J. Am. Chem. Soc.* **2008**, *130*, 3502–3503.
(35) Fritz, S. E.; Martin, S. M.; Frisbie, C. D.; Ward, M. D.; Toney, M. F. *J. Am. Chem. Soc.* **2004**, *126*, 4084–4085.
(36) Mullen, K.; Wegner, G. *Electronic Materials: The Oligomer Approach*; Wiley-VCH: New York, 1998.
(37) Frimer, A. A. *Chem. Rev.* **1979**, *79*, 359–387.

Summary and Conclusions

We have reported the synthesis of new highly soluble oligothiophenes with thermally labile solubilizing groups and utilized ester thermolysis not only to afford a thin film morphological transformation but also to extend the conjugation of oligothiophene cores to include styryl end groups. Analysis of the films by NEXAFS and GIXD revealed their edge-on orientation and high in-plane crystallinity. The stability of α,ω-distyryl oligothiophenes appears to be tied to the elimination of reactive sites in the conjugated molecule, which suggests that oligothiophenes can be rendered highly resistant to oxidative degradation through judicious choice of end-group structures. This improvement in structural design allows the favorable combination of solution deposition facilitated by thermally labile solubilizing groups and air stability offered by α,ω-distyryl oligothiophenes, which greatly simplifies processing conditions for organic electronics.

Acknowledgment. This work was supported by the Director, Office of Science, Office of Basic Energy Sciences, Materials Sciences and Engineering Division, of the U.S. Department of Energy under Contract DE-AC02-05CH11231. Portions of this research were carried out at the Stanford Synchrotron Radiation Laboratory, a national user facility operated by Stanford University on behalf of the U.S. Department of Energy, Office of Basic Energy Sciences. We acknowledge Daniel Poulsen for assistance with DFT calculations.

Supporting Information Available: Complete experimental procedures and characterization of **1**−**4** and **preDS4T**, **preDS5T**, and **preDS6T** (PDF). This material is available free of charge via the Internet at http://pubs.acs.org.

CM900267V